



# Numerical investigation of the dynamical environment of 65803 Didymos

L. Dell'Elce<sup>a,\*</sup>, N. Baresi<sup>b</sup>, S.P. Naidu<sup>c</sup>, L.A.M. Benner<sup>c</sup>, D.J. Scheeres<sup>b</sup>

<sup>a</sup> *Université de Liège, 4000 Liège, Belgium*

<sup>b</sup> *University of Colorado Boulder, 80309 Boulder, CO, United States*

<sup>c</sup> *Jet Propulsion Laboratory, California Institute of Technology, 91109 Pasadena, CA, United States*

Received 23 September 2016; received in revised form 8 December 2016; accepted 15 December 2016

Available online 28 December 2016

## Abstract

The Asteroid Impact & Deflection Assessment (AIDA) mission is planning to visit the Didymos binary system in 2022 in order to perform the first demonstration ever of the kinetic impact technique. Binary asteroids are an ideal target for this since the deflection of the secondary body can be accurately measured by a satellite orbiting in the system. However, these binaries offer an extremely rich dynamical environment whose accurate investigation through analytical approaches is challenging at best and requires a significant number of restrictive assumptions. For this reason, a numerical investigation of the dynamical environment in the vicinity of the Didymos system is offered in this paper. After computing various families of periodic orbits, their robustness is assessed in a high-fidelity environment consisting of the perturbed restricted full three-body problem. The results of this study suggest that several nominally stable trajectories, including the triangular libration points, should not be considered as safe as a state vector perturbation may cause the spacecraft to drift from the nominal orbit and possibly impact one of the primary bodies within a few days. Nonetheless, there exist two safe solutions, namely terminator and interior retrograde orbits. The first one is adequate for observation purposes of the entire system and for communications. The second one is more suitable to perform close investigations of the primary body.

© 2016 COSPAR. Published by Elsevier Ltd. All rights reserved.

**Keywords:** Didymos; AIDA mission; Restricted three-body problem

## 1. Introduction

Current estimates indicate that  $15 \pm 4\%$  of the Near-Earth Asteroid (NEA) population is made of binary systems (Margot et al., 2002; Pravec et al., 2006, 2016). Thus, it is not surprising that several spacecraft missions have been envisaged to explore asteroid pairs in the Solar System.

A notable example is the Asteroid Impact & Deflection Assessment (AIDA) mission (Cheng et al., 2015): an inter-

national collaboration between NASA and ESA consisting of two spacecraft to be launched in 2020 towards the binary asteroid 65803 Didymos (Benner et al., 2010). The ESA satellite, also known as the Asteroid Impact Mission (AIM), will arrive first to characterize the dynamical environment in the proximity of the target binary and will prepare for the arrival of the NASA spacecraft, the Double Asteroid Redirect Test (DART). DART's mission is to impact at 6.25 km/s against the smaller of the primary bodies, named 'secondary' hereafter, thereby performing the first ever experiment of the kinetic impactor technique. At the time of impact, AIM will be observing the collision and collect valuable data to determine any changes in the

\* Corresponding author.

E-mail address: [lamberto.dellelce@ulg.ac.be](mailto:lamberto.dellelce@ulg.ac.be) (L. Dell'Elce).

orbital pattern and internal structure of the secondary body. This will be done in conjunction with data provided by additional landers and 3U CubeSats to be deployed upon arrival at the destination in safe operating locations that are yet to be selected. This is because the dynamical environment about binary asteroids is so challenging that the existence of orbits where the satellites would be bound to either of the bodies is actually still open to debate.

The main problem encountered in modeling the dynamics about binary asteroids is that the orbit of the secondary body about the primary is strongly non-Keplerian due to irregular shapes, spin-orbit coupling, and the influence of solar radiation pressure (SRP) and solar gravity. In addition, according to the current model (ESA, 2015), the secondary body orbits around the primary in an equatorial orbit with an estimated eccentricity of 0.03. This already eliminates a great number of candidate periodic orbits that can be found in the vast literature concerning the circular restricted three-body problem (CR3BP) (Szebehely, 1967).

All of these forces yield a very rich dynamical environment that was the subject of several investigations found in literature. Scheeres and Bellerose laid out the foundation of what is now known as the restricted Hill full four-body problem (RHF4BP) by deriving the equations of its closest approximations, i.e., the restricted Hill four-body problem (RH4BP) and the restricted full three-body problem (RF3BP) (Scheeres and Bellerose, 2005). Here, ‘restricted’ denotes that one body, namely the spacecraft, is massless and, as such, it does not affect the motion of the binary, while ‘full’ indicates that the attitude and orbital dynamics of the attractors are coupled. In particular, the authors modeled the shape of one of the two primaries as a tri-axial ellipsoid, thereby showing for the first time that the irregular mass distribution of the asteroids significantly affected the stability of CR3BP-based solutions. Similar results were also obtained in Gabern et al. (2006) using Hamiltonian formalism and normal forms. Here, the primaries were approximated as a sphere and a three-mascon rigid body in a T configuration admitting stable regions of motion, despite the tidal force of the Sun being taken into account. Indeed, periodic orbits in the RF3BP were also found in Bellerose and Scheeres (2005), where the primaries were considered to be in a *long-axis* configuration, i.e., the secondary was in a relative equilibrium with a primary ellipsoid along its minimum axis of inertia. Yet, none of the computed solutions in both Gabern et al. (2006) and Bellerose and Scheeres (2005) included the effects of SRP, which is known to be significant in the vicinity of small bodies (Bellerose et al., 2009).

For all these reasons, in this paper we envision a fully numerical approach describing the motion of a mass particle subject to the gravitational attraction of a constant-density polyhedron (the primary) (Naidu et al., 2016) and a constant-density tri-axial ellipsoid (the secondary), while being perturbed by the third-body attraction of the Sun

and cannonball SRP. The model, hereby referred to as the perturbed restricted full three-body problem (PRF3BP), is applied to investigate the dynamical environment in the proximity of the binary asteroid 65803 Didymos and assess whether regions of robust motion can be found in the system.

To improve the realism of our simulations, we also account for second-order effects on the orbital motion of the smaller body about the primary due to its shape, the eccentricity of the secondary orbit, and the oblateness of the primary body (McMahon and Scheeres, 2013). These effects induce librations of the secondary as seen in the corotating frame of the primaries that can destabilize motion in the proximity of DART’s target. This is observed for several types of orbits about the smaller body that could be potential candidates for the AIM mission. Therefore, the inclusion of secondary shape and attitude, eccentricity, and oblateness effects is paramount for the purposes of our analysis.

Finally, targeting robust orbital regions, several candidate trajectories are considered, including triangular libration points, planar symmetric periodic orbits derived from the CR3BP, and terminator orbits (Scheeres, 1999). All of the considered trajectories are tested with a Monte Carlo simulation that runs different realizations of Didymos orbital and physical parameters as specified in ESA (2015). The results of the numerical investigation are shown in Section 4 after reviewing the equations of motion implemented in our high-fidelity orbit propagator in Section 2 and the proposed candidate trajectories in Section 3. Additional results on the identified robust orbits are finally provided in Section 5. Conclusions are given in Section 6.

## 2. Dynamical environment

This section offers a brief overview of the dynamical environment that was used to perform high-fidelity simulations. The definition of the reference frames and relevant transformations used herein is disclosed in Appendix A.

Following the notation in Scheeres and Bellerose (2005), the dynamics of the satellite within the Didymos system is modeled via the PRF3BP. Here, ‘perturbed’ means that additional perturbations acting on the spacecraft are considered. Specifically, we consider non-spherical mass distribution of the primaries, SRP, and third-body attraction of the Sun. Most equations of the PRF3BP and of more advanced systems are derived in Scheeres and Bellerose (2005).

Dimensionless quantities are used in this paper. Denote by  $m_1$  and  $m_2$  the masses of the attractors, and by  $G$  the universal gravitational constant. Length and time are normalized by means of the nominal semi-major axis of the binary orbit,  $a$ , and of the inverse nominal mean motion,  $\sqrt{\frac{a^3}{G(m_1+m_2)}}$ , respectively. We note that the secondary com-

pletes one orbital revolution about the primary in  $2\pi$  as the mean motion in normalized units is now equal to  $n = 1$ . Dimensionless inertia of the attractors is obtained by using the coefficients  $m_j a^2$ , with  $j = 1, 2$  for the primary and secondary body, respectively.

The equations of motion (EoM) are integrated by means of the MATLAB solver *ode113*, which is a variable-order and step-size Adams-Bashforth-Moulton integrator (Shampine and Reichelt, 1997). The relative tolerance of the adaptive step is set to  $10^{-13}$ .

### 2.1. Binary dynamics

Evaluating the coupled attitude and orbital motion of two arbitrarily-shaped masses can be computationally intense and it adds unnecessary complexity for the scope of the paper. For this reason, three assumptions are introduced to simplify the problem without losing the fundamental dynamics:

- The spin of the bodies is parallel to their orbital momentum, i.e.,  $\hat{Z}_C \parallel \hat{Z}_1 \parallel \hat{Z}_2$ , as shown in Fig. 1.
- The secondary is modeled as a tri-axial ellipsoid with  $I_{2,x}$ ,  $I_{2,y}$ , and  $I_{2,z}$  as the moments of inertia along the principal axes. The primary is modeled as an oblate spheroid, so that  $I_{1,x} = I_{1,y} = I_{1,eq}$  and the inertia about the polar axis is  $I_{1,z}$ .
- The main body has constant spin,  $\omega_1 \hat{Z}_1$ .

These assumptions are in good agreement with the current radar observations of the Didymos system, which suggest that the primary is roughly spheroidal and synchronous rotations of the secondary are likely (Naidu et al., 2016). Indeed, the same hypotheses were made in the current reference model provided by ESA (2015).

Based on the aforementioned assumptions, a reduced-order system modeling the full two-body problem can be derived as in McMahon and Scheeres (2013). Denote by  $d, \phi$ , and  $\theta$  the distance between the barycenters of the attractors, the libration of the secondary and the argument of latitude, respectively. This notation is illustrated in Fig. 2. Their EoM are (McMahon and Scheeres, 2013)

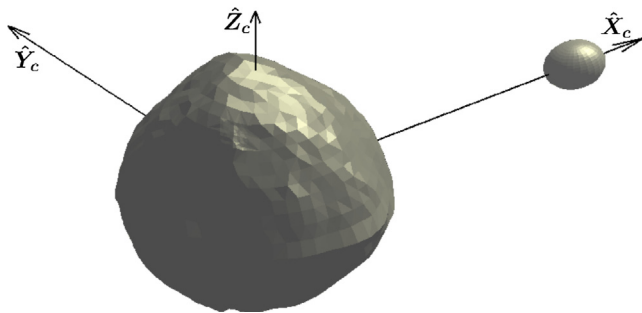


Fig. 1. Co-rotating reference frame. The origin coincides with the barycenter of the Didymos system.

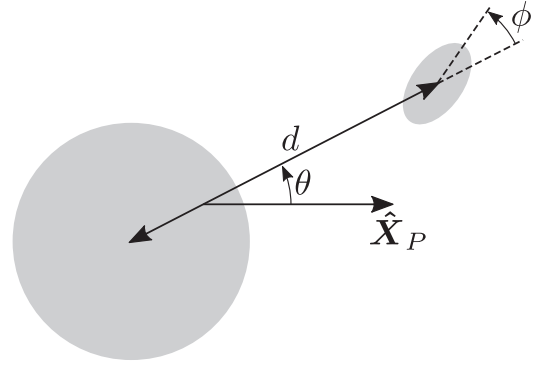


Fig. 2. Reduced DoF of the binary orbit as viewed from the  $\hat{Z}_P$  axis.

$$\begin{aligned} \ddot{d} &= \left( \frac{K - I_{2,z} \dot{\phi}}{I_{2,z} + \mu d^2} \right)^2 d - \frac{1}{\mu} \frac{\partial V}{\partial d}, \\ \ddot{\phi} &= 2 \frac{K - I_{2,z} \dot{\phi}}{I_{2,z} + \mu d^2} \frac{\dot{d}}{d} - \left( \frac{1}{\mu d^2} + \frac{1}{I_{2,z}} \right) \frac{\partial V}{\partial \phi}, \\ \dot{\theta} &= \frac{K - I_{2,z} \dot{\phi}}{I_{2,z} + \mu d^2}, \end{aligned} \tag{1}$$

where dots denote derivatives with respect to the dimensionless time and  $\mu = \frac{m_2}{m_1 + m_2}$  denotes the mass parameter. The mutual potential,  $V$ , is given by

$$\begin{aligned} V(d, \phi) = -\frac{\mu}{d} \left\{ 1 + \frac{1}{2d^2} \left[ (I_{1,z} - I_{1,eq}) - \frac{1}{2} (I_{2,x} + I_{2,y}) \right. \right. \\ \left. \left. + I_{2,z} + \frac{3}{2} (I_{2,y} - I_{2,x}) \cos 2\phi \right] \right\}, \end{aligned}$$

and the free angular momentum,  $K$ , is an integral of motion that follows from the independence of the system Lagrangian with respect to the argument of latitude  $\theta$ . The constant value of  $K$  is deduced from the initial states by solving the last of Eqs. (1) for the free angular momentum itself, i.e.,

$$K = (I_{2,z} + \mu d^2(0)) \dot{\theta}(0) + I_{2,z} \dot{\phi}(0).$$

In the context of the elliptic restricted three-body problem (ER3BP), the binary orbit is usually assumed to be Keplerian with librations of the secondary body due to simple kinematics relationships. In contrast, the model discussed in this section yields a dynamical coupling between the libration angle and the distance between the centers of mass of the two attractors that may lead to unstable oscillations. Sufficient conditions for the boundedness of the librations of the secondary in this model are assessed in McMahon and Scheeres (2013). All the simulations performed in this work are such that these conditions are satisfied.

### 2.2. Spacecraft dynamics

Denote by  $\mathbf{r} = [x, y, z]^T$  the position vector of the satellite in the co-rotating frame  $\mathcal{C}$  illustrated in Fig. 1. The EoM of  $\mathbf{r}$  are:

$$\begin{aligned}
\ddot{x} - \ddot{\theta}y - 2\dot{\theta}\dot{y} &= \dot{\theta}^2 x - \frac{(1-\mu)(x+\mu d)}{r_1^3} - \frac{\mu[x-(1-\mu)d]}{r_2^3} + f_x, \\
\ddot{y} + \ddot{\theta}x + 2\dot{\theta}\dot{x} &= \dot{\theta}^2 y - \frac{(1-\mu)y}{r_1^3} - \frac{\mu y}{r_2^3} + f_y, \\
\ddot{z} &= -\frac{(1-\mu)z}{r_1^3} - \frac{\mu z}{r_2^3} + f_z.
\end{aligned} \tag{2}$$

Here,  $r_1$  and  $r_2$  are the distances of the satellite from the barycenter of the attractors, and  $\mathbf{f} = [f_x, f_y, f_z]^T$  is the perturbing force.

Three perturbations are included in  $\mathbf{f}$ . First, non-spherical attractors are considered. Specifically, a constant-density polyhedron (Werner and Scheeres, 1996) and a constant-density tri-axial ellipsoid (Scheeres, 1994) are used to model the gravitational force of the primary and secondary body, respectively. The shape model of the primary is roughly spheroidal and has a volume equivalent diameter of about 780 m (Naidu et al., 2016). The primary is slightly oblate and has a nominal  $J_2$  value of approximately 0.001 under a uniform density assumption. It has an equatorial ridge similar to (but not as prominent as) the ones seen on the primaries of other binary and triple systems such as 1999 KW4 (Ostro et al., 2006), 1994 CC (Brozović et al., 2011), and 2000 DP107 (Naidu et al., 2015). The equatorial ridge is somewhat irregular and has a  $\sim 300$  m long facet. The primary shape model is defined by 1000 vertices and 1996 triangular facets with an effective resolution of  $\sim 50$  m. Visible range extents of the secondary in radar delay-Doppler images suggest a diameter between 150 and 180 m (Naidu et al., 2016). The radar data also suggest that the secondary spin is, on average, synchronous with the binary orbit. Second, a *cannonball* model is used to model the SRP, i.e., the force is systematically directed in the opposite direction of the Sun, whereas the magnitude scales as the inverse of the squared distance between the spacecraft and the Sun itself. Finally, solar gravity is also accounted for. To compute the two latter perturbations, we assume that the heliocentric orbit of Didymos is Keplerian and characterized by the orbital elements listed in Table 1.

### 3. Candidate trajectories

Various orbits are considered as possible trajectories for the AIM satellite in the Didymos system. Some results could potentially be of use for the CubeSats ejected by the mother-craft, as well. These solutions are computed under several assumptions, so that their robustness in the high-fidelity environment needs to be later assessed as in Section 4.

We stress that this survey is not comprehensive and it is limited to candidates which are considered to be of interest for the AIDA mission. For example, Halo orbits or planar orbits about collinear libration points are neglected because they are either unstable or not robust with respect to the various perturbations discussed in Section 2.

Table 1  
Parameters of the Didymos system.

	Value	Units
<i>Physical parameters</i>		
Mass parameter, $\mu$	$9.214 \cdot 10^{-3}$	–
Total mass	$5.278 \cdot 10^{11}$	kg
Primary ellipsoid semi-axes	399, 392, 380	m
Secondary ellipsoid semi-axes	103, 79, 66	m
Primary spin rate	$7.723 \cdot 10^{-4}$	rad/s
<i>Binary orbit</i>		
Semi-major axis	1180	m
Pole ecliptic longitude	310	deg
Pole ecliptic latitude	–84	deg
<i>Heliocentric orbit</i>		
Semi-major axis	1.645	AU
Eccentricity	0.384	–
Inclination	3.408	deg
Argument of perigee	319.20	deg
RAAN	73.256	deg
Mean anomaly	195.97	deg
Epoch	2007/01/31	UTC

#### 3.1. Triangular libration points

The first candidate solution are the triangular libration points  $L_4$  and  $L_5$ , i.e., the two equilibrium points in the co-rotating frame that do not lie on the  $\hat{X}_C$  axis (Arnold et al., 1993, Chap. 2.5). These points are stable in the framework of the CR3BP. Nonetheless, stability is no more guaranteed for low mass ratio when non-spherical attractors are considered (Scheeres and Bellerose, 2005).

Libration points cannot be rigorously defined in the high-fidelity environment because of the presence of external perturbations and eccentricity effects. Hence, they are computed by assuming that the primary and the secondary are a point mass and a tri-axial ellipsoid, respectively. In addition, SRP, and third-body attraction of the Sun are neglected and it is assumed that  $\dot{d}(t) = \phi(t) = 0 \forall t > 0$ .

Under these hypotheses, the triangular points of Didymos are located at  $0.491\hat{X}_C \pm 0.866\hat{Y}_C$ . The associated linearized systems admits two pairs of complex conjugate eigenvalues, namely  $\pm 0.97i$  and  $\pm 0.26i$ , so that these equilibria are stable, which makes them a suitable candidate for the robustness analysis. A parametric study on the stability of libration points under the assumptions of this section is discussed in Scheeres (2012, Chap. 9.3).

#### 3.2. Symmetric planar periodic orbits

Planar orbits are of interest because of their proximity to one or both primaries, which makes them suitable for a thorough inspection of the system. Here, we only consider trajectories that are symmetric with respect to the  $\hat{X}_C$  axis.

Periodic solutions are computed by means of the predictor-corrector algorithm detailed in Baresi et al. (2016) and Scheeres (2012). Solutions in the high-fidelity environment discussed in Section 2 would be isolated, at

best, because of the multiple time-dependent forcing terms appearing in the term  $f$  of Eq. (2). Hence, the same assumptions introduced in Section 3.1 are used to find periodic orbits.

Five families were identified, namely: direct interior, direct exterior, retrograde interior, retrograde exterior, and circum-secondary retrograde orbits (CSO). The stability of direct and retrograde interior and exterior orbits was studied in the context of the 1999 KW4 binary system (Scheeres, 2012, Chap. 9.4) under the same assumptions discussed herein. CSO are well known stable orbits of planetary binary systems, where they are named distant retrograde orbits, but, to the best of our knowledge, their stability was never studied in the context of small bodies.

Direct orbits have the advantage to exhibit a slower dynamics in the co-rotating frame. For the same reason, they are also more prone to be significantly affected by the gravitational perturbations of the two primaries. Fig. 3 depicts a sample trajectory for each of them. Here, dots denote the  $x$ -axis crossing, i.e., the location on the  $\hat{X}_C$  axis corresponding to the crossing of the surface of sec-

tion that we used to enforce the periodicity of the orbit. Direct exterior orbits are apparently retrograde when observed in the co-rotating frame.

The  $x$ -axis crossing and the associated tangential velocity of the solutions are depicted in Fig. 4(a). Because of the symmetries of the problem, these two components fully identify the orbit. The largest part of the branch of direct interior orbits is characterized by two solution for the same  $x$ -axis crossing at different velocities, whereas all the other families can be parametrized by means of the  $x$ -axis crossing only. The stability indices of the considered periodic orbits are shown in Fig. 4(b) as a function of the  $x$ -axis crossing location. Each of them is defined as the sum of one pair of reciprocal non-unitary eigenvalues of the monodromy matrix (Howell, 1984), which explains the occurrence of two lines per initial conditions. The orbit is stable when all of the stability indices are real and smaller than 2. The entire branches of direct interior orbits and CSO are stable. However, the proximity of the indices of high-velocity direct interior orbits and large CSO to the stability bounds makes their robustness questionable. Both

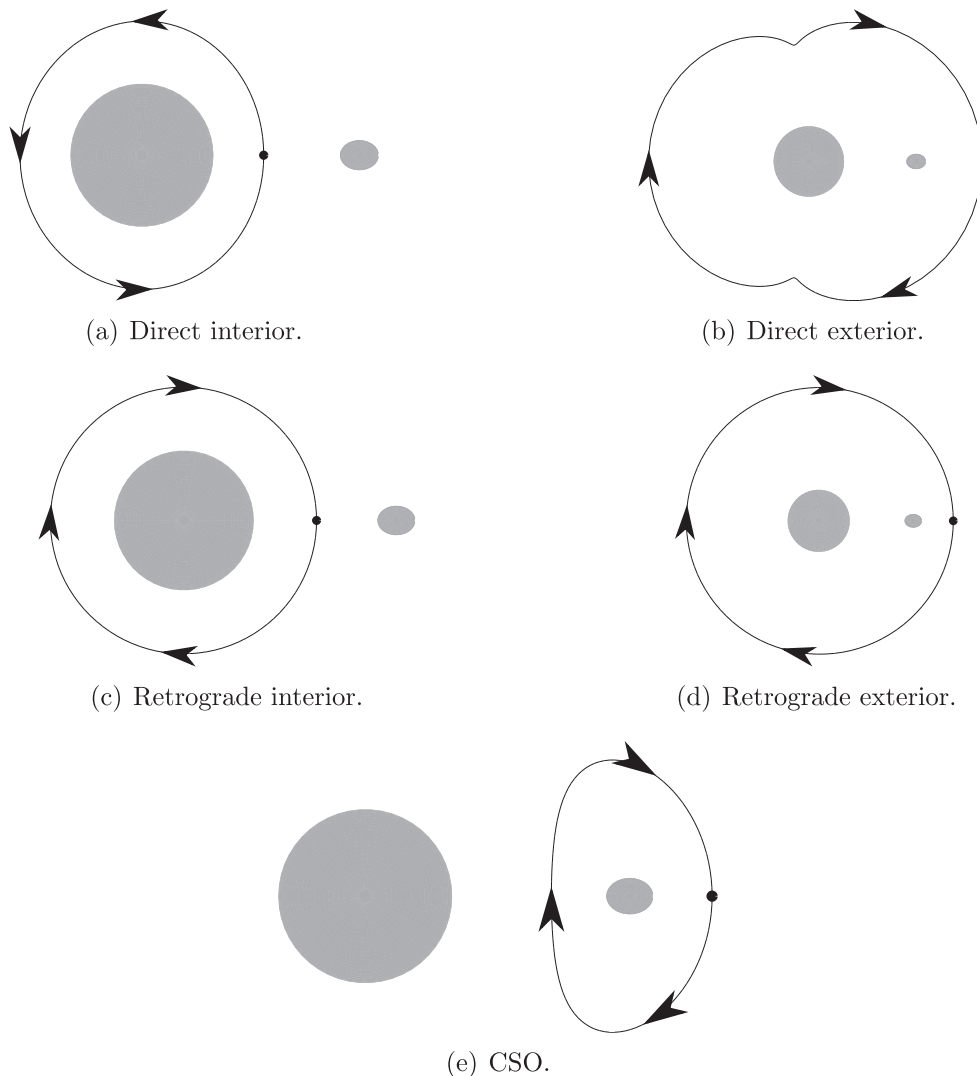
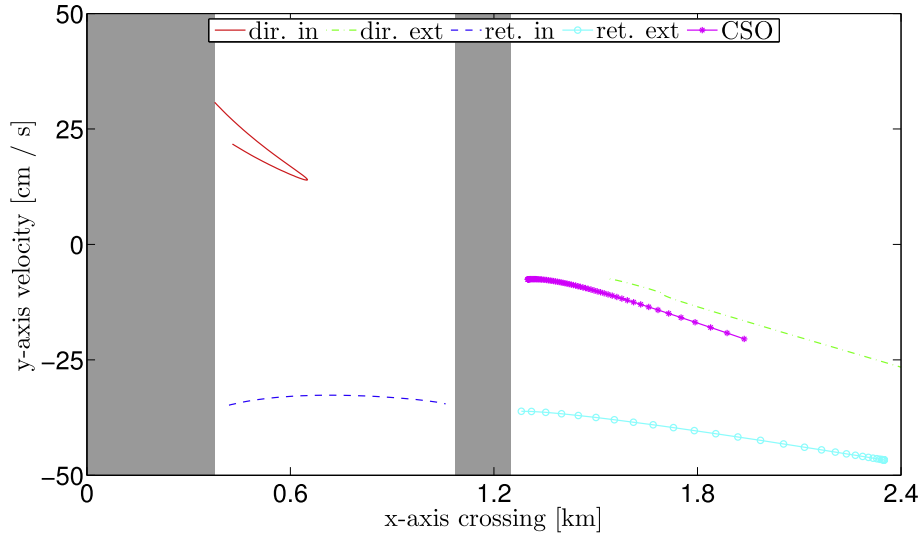
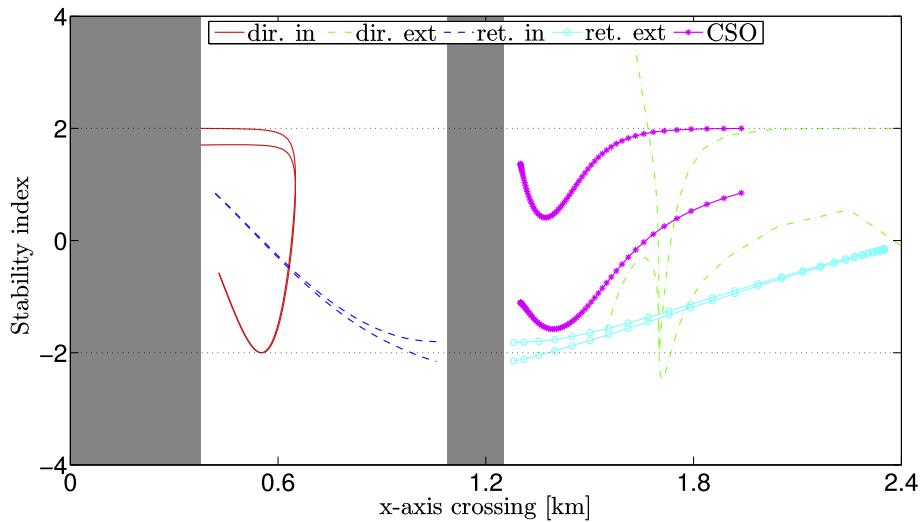


Fig. 3. Sample of each family of planar symmetric orbits in the corotating frame.



(a) Velocity at the crossing of the surface of section.



(b) Stability indices. Dotted lines denote stability bounds.

Fig. 4. Families of planar symmetric orbits. Shaded regions denote the encumbrance of the primaries.

interior and exterior retrograde orbits are mostly stable if fairly distant from the secondary body. Finally, only direct exterior orbits sufficiently far from the secondary are stable. All unstable solutions are neglected in the robustness analysis of Section 4.

### 3.3. Terminator orbits

Terminator orbits offer a privileged position for observing the overall binary system and for communication purposes between a mothercraft and other satellites located, for example, in the planar orbits described in Section 3.2 or landed on a primary body.

Terminator orbits are such that the orbital angular momentum points toward the Sun direction, as illustrated in Fig. 5. The required rotation of the right ascension of

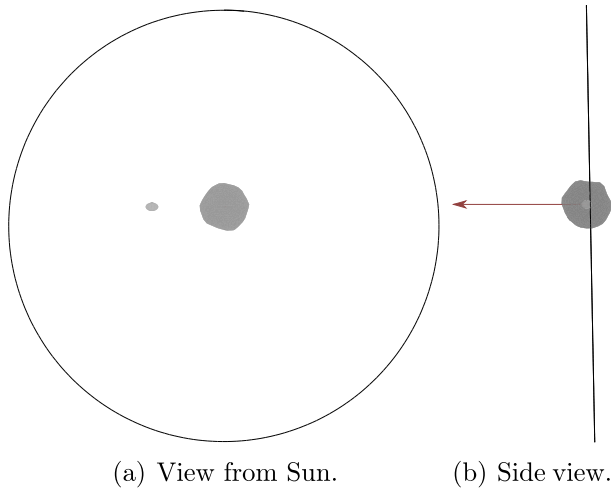
the ascending node (RAAN) is achieved by means of the SRP.

In this work, terminator orbits are computed by assuming that the satellite is only subject to the point-mass gravity of Didymos and SRP.

For a desired semi-major axis,  $a$ , frozen orbit conditions are met by choosing the orbital eccentricity as in Scheeres (1999):

$$e = \cos \left[ \tan^{-1} \left( \frac{3}{2} \frac{C_r}{B} \frac{\Phi}{c} \sqrt{\frac{a}{\mu \mu_{\odot} a_H (1 - e_H^2)}} \right) \right],$$

where  $\mu$  and  $\mu_{\odot}$  are the Didymos and solar gravitational parameters, respectively,  $a_H$  and  $e_H$  denote the semi-major axis and eccentricity of the heliocentric orbit, respectively,  $C_r$  is the reflectivity coefficient,  $B$  is the satellite's mass to cross sectional area ratio,  $\Phi = 1367 \text{ W m}^{-2}$  indicates the solar flux at 1 AU, and  $c$  is the speed of light.



the maximum semi-major axis of the terminator orbit that should be considered for the robustness analysis of Section 4.

In the high-fidelity simulations, the frozen orbit is initialized as a Keplerian orbit about the total mass of the system. Various semi-major axes are tested to investigate the minimum distance from Didymos at which the satellite can be safely placed.

**4. Robustness analysis**

The robustness of the solutions discussed in Section 3 is now assessed by means of a Monte Carlo (MC) analysis. Various uncertainty sources are considered for this purpose, namely:

- the initial eccentricity of the binary orbit,  $e(0)$ ;
- the initial longitude of the secondary body,  $\theta(0)$ ;
- the initial libration of the secondary body,  $\phi(0)$ ;
- satellite properties, namely the reflectivity coefficient,  $C_r$ , and the mass to cross sectional area ratio,  $B$ .

Uniform distributions are used to model the marginal probability density function (PDF) of each variable in agreement with the maximum entropy principle (Shannon, 1948). Typical values of past missions to asteroids detailed in Scheeres (2012) are used for the bounds of  $B$ . The five uncertainty sources are assumed to be uncorrelated. Fig. 7 summarizes the probabilistic modeling of the sources.

We note that the support of most uncertainty sources is likely to be reduced when more detailed information on Didymos will be available. For this reason, the results presented in this section are reasonably conservative.

The probability of impacting one of the attractors or of escaping the Didymos system is determined by propagating 1000 trajectories from as many independent identically dis-

Fig. 5. Example of a terminator orbit. The red arrow points toward the Sun. (For interpretation of the references to color in this figure legend, the reader is referred to the web version of this article.)

If the desired semi-major axis is excessively large, the action of the SRP may tear off the satellite from the Didymos system. A sufficient condition for the stability of the terminator orbit derived in Scheeres (2012, Chap. 12) states that  $a$  should be chosen to satisfy

$$a \leq \frac{1}{4} \sqrt{\frac{\mu}{\max(|f_{srp}|)}}, \tag{3}$$

where  $f_{srp}$  denotes the specific force due to the SRP. In the same reference, an alternative necessary and sufficient condition, which was derived in a completely different framework than Eq. (3), states that the maximum semi-major axis should be no larger than  $\sqrt{3}$  times the outcome of Eq. (3). Fig. 6 depicts the maximum semi-major axis according to these two criteria as a function of  $\frac{B}{C_r}$  for the Didymos system. This diagram can be used to estimate

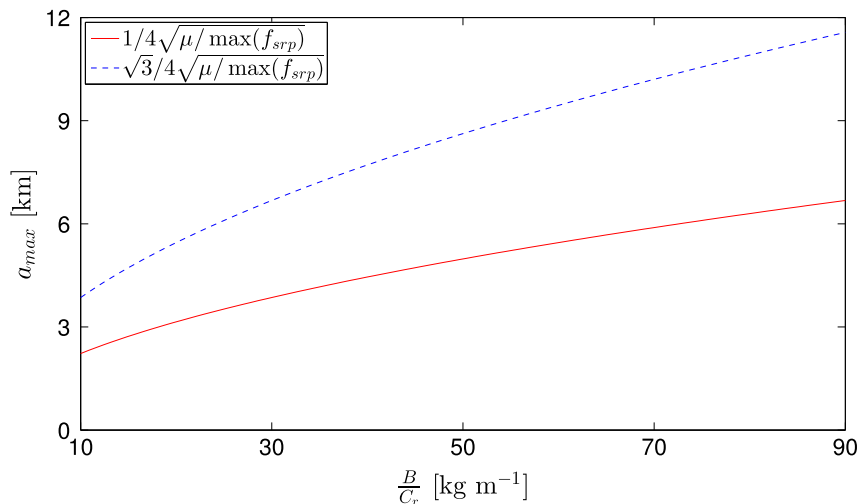


Fig. 6. Maximum semi-major axis of the terminator as a function of the SRP.

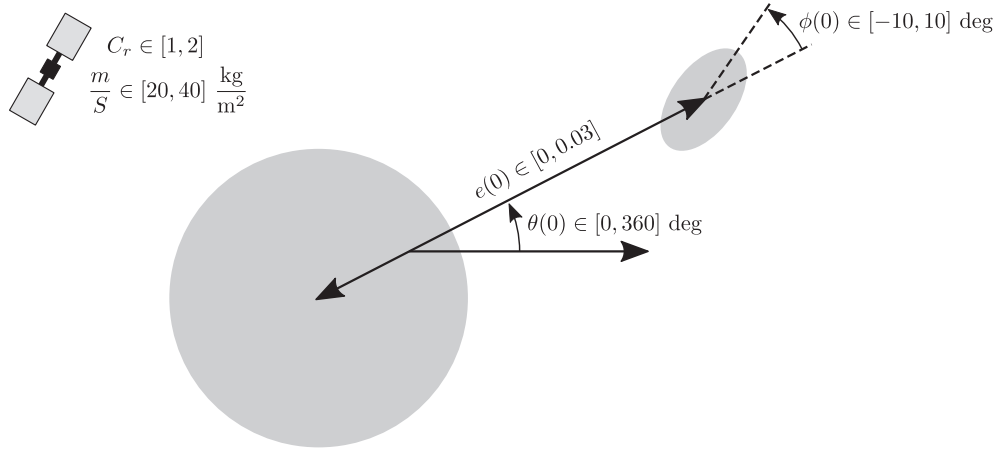


Fig. 7. Uncertainty sources. All of them are modeled by means of uniform distributions with range indicated in the figure.

tributed samples of the aforementioned sources. This number of samples results from a trade-off between convergence of the results and computational cost. We systematically check that 1000 samples yield a satisfactory convergence of the probability of interest to derive our conclusions. Specifically, we verify that the convergence of any variable of interest is within 1% at  $3\sigma$  confidence for all the identified robust orbits. For each sample of the uncertain set, the numerical integration of the EoM is stopped whenever

- the spacecraft enters the circumscribing sphere surrounding the primary body,
- the spacecraft enters the circumscribing sphere surrounding the secondary body, or
- the spacecraft escapes from the system, i.e., its distance from the barycenter exceeds the radius of the Hill's sphere of influence,

$$a_H(1 - e_H) \left( \frac{\mu}{3\mu_\odot} \right)^{1/3},$$

where  $\mu$  and  $\mu_\odot$  denote the Didymos and Solar gravitational parameters, respectively.

For the sake of conciseness, we refer to these three events as ‘failure’. If failure does not occur, the simulation is stopped after either  $t_S = 30$  days for the triangular libration points and planar orbits, or  $t_S = 400$  days for the terminator orbits, owing to their slower dynamics.

Our goal is to find ‘safe’ stable trajectories in the sense that they do not fail almost surely before a prescribed time  $t_S$ , i.e.,

$$\text{find } [\mathbf{r}_0, \dot{\mathbf{r}}_0] \text{ such that } P_{\text{failure}}(\mathbf{r}_0, \dot{\mathbf{r}}_0, t_S) = 0, \quad (4)$$

where  $[\mathbf{r}_0, \dot{\mathbf{r}}_0]$  are the initial position and velocity vectors of the propagated object, and  $P_{\text{failure}}$  is defined as

$$P_{\text{failure}}(\mathbf{r}_0, \dot{\mathbf{r}}_0, t) = \Pr(t_{\text{failure}} \leq t | \mathbf{r}(0) = \mathbf{r}_0, \dot{\mathbf{r}}(0) = \dot{\mathbf{r}}_0).$$

Here,  $\Pr(a|b)$  denotes the probability of the event  $a$  given the event  $b$ , and  $t_{\text{failure}}$  is the time when a failure occurs.<sup>1</sup> For the sake of conciseness, we use the short-hand notation  $P_{\text{failure}}(t)$  whenever possible. In what follows,  $P_{\text{failure}}$  is estimated for each considered pair of  $\mathbf{r}_0$  and  $\dot{\mathbf{r}}_0$  by means of the MC propagation where the number of failing trajectories is divided by the number of samples.

Indeed, Eq. (4) is ill posed and it may admit either none, one, or infinite solutions depending on the effects and range of the uncertainty sources.

We only consider the natural dynamics of the satellite, i.e., active control to maintain the orbit is neglected. The epoch of the simulation is set to the nominal beginning of the AIDA mission operations, namely April 1st, 2022. The other parameters of the Didymos system are detailed in ESA (2015) and summarized in Table 1.

#### 4.1. Triangular libration points

Fig. 8 depicts the probability of failure as a function of the desired mission window  $t$ , showing that the 60% of the sample trajectories did not survive for more than 30 days. Interestingly,  $P_{\text{failure}}(t)$  is non-negligible for mission windows of the order of 1 day, which roughly corresponds to two orbital revolutions of the secondary body about the primary. This performance would further deteriorate if uncertainty in the injection velocity were accounted for.

In this study, the eccentricity of the binary orbit is an uncertainty source and libration points are computed by neglecting it, as discussed in Section 3.1. The robustness of these points may be possibly enhanced if the eccentricity is known and it is accounted for in the definition of the dynamical substitutes that appear in the corresponding ER3BP. Regardless, the importance of the eccentricity and initial longitude of the binary orbit is hereby disclosed

<sup>1</sup> Note that  $t_{\text{failure}} \rightarrow \infty$  for stable orbits that are robust with respect to the entire uncertain set.

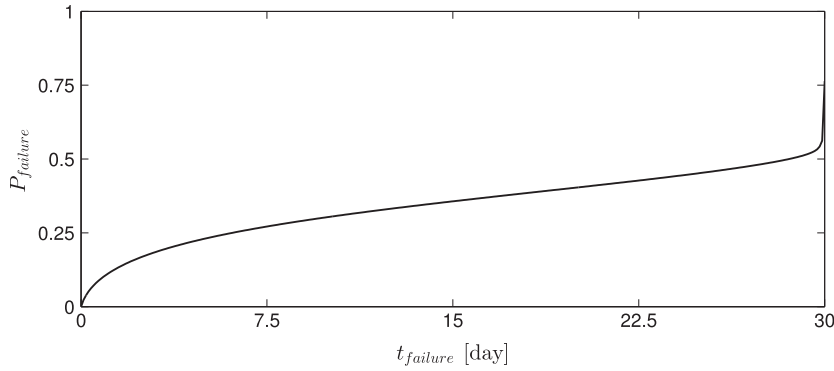
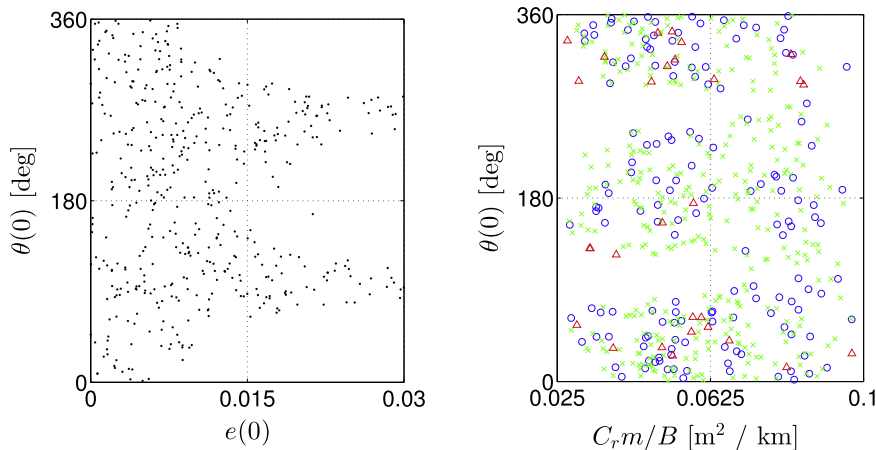


Fig. 8. Probability of failure as a function of the mission window when the satellite is initially parked in  $L_4$ .



(a) Survived samples after 30 days.

(b) Failure events. Crosses, circles, and triangles denote impacts on primary, secondary, and escape, respectively.

Fig. 9. Relevant correlations for the successful and failing samples after 30 days when the satellite is initially parked in  $L_4$ .

in Fig. 9(a), which shows the values of these variables for the non-failing samples. No successful sample exists for high eccentricity when the initial longitude is such that the secondary is close to the periaapsis or apoapsis of the binary’s orbit. Similarly, success is only systematically achieved for very low SRP and initial longitude close to 90 or 270 deg, as depicted in Fig. 9(b).

Analogous results are obtained for  $L_5$ . Therefore, we conclude that triangular libration points are not good candidates for the purposes of the AIDA mission.

#### 4.2. Symmetric planar periodic orbits

The MC propagation of the uncertainty sources was applied to five members of each family introduced in Section 3.2. Figs. 10–17 illustrate their probability of failure before 30 days and relevant correlations between failure events and uncertainty sources. The size of the attractors is depicted to provide graphical insight in the distance of the orbits from the primaries. The graphics of the probability of failure of direct interior orbits is different because of

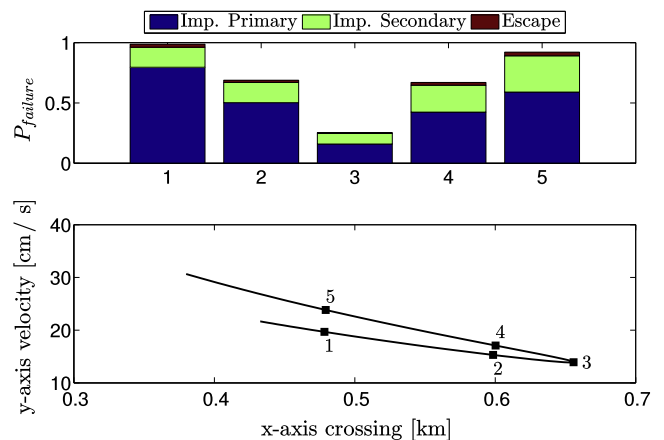


Fig. 10. Probability of failure of direct interior orbits.

the non-monotonicity of the branch as a function of the  $x$ -crossing.

Direct interior orbits generally fail by impacting the main body, as shown in Fig. 10. Here,  $P_{failure}(30 \text{ day})$  is minimized when the  $x$ -axis crossing of the family occurs

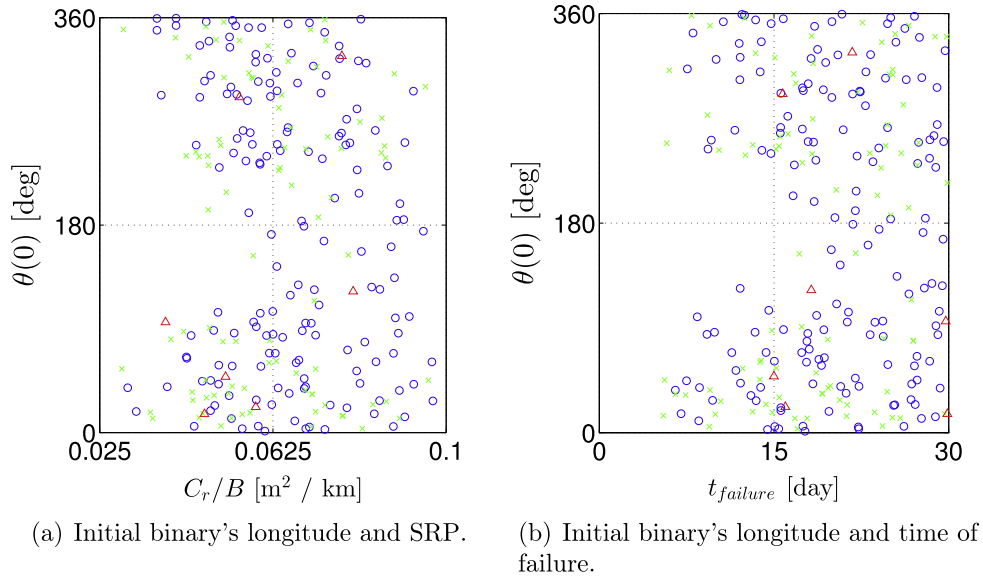


Fig. 11. Failure events of the third direct interior orbit. The same symbol convention of Fig. 9(b) is used.

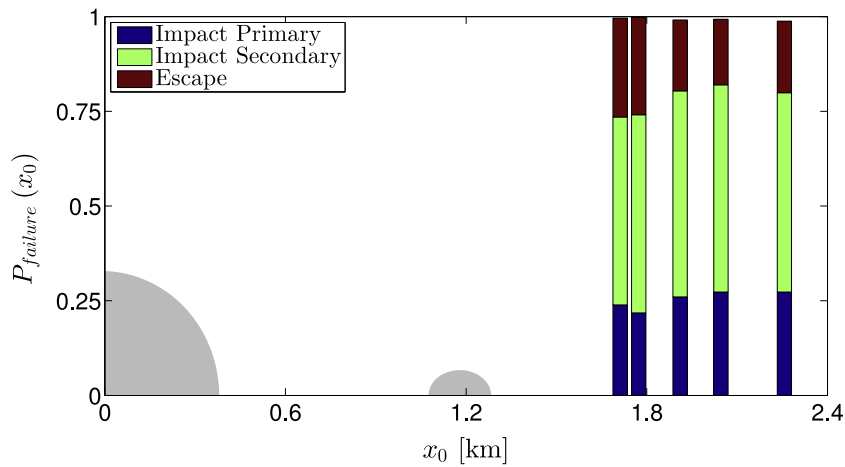


Fig. 12. Probability of failure of direct exterior orbits.

at the farthest distance from the primary body. If the  $C_r$  to  $B$  ratio is low and the orbit is initiated when the secondary is close to its apoapsis, no failure is observed, as shown in Fig. 11(a). Furthermore, Fig. 11(b) discloses that the second condition is beneficial in general as it doubles the minimum time of failure.

According to Figs. 12 and 15, all direct and retrograde exterior orbits have nearly 100% probability of failure, which is mainly due to the occurrence of an impact with the secondary body. Although these orbits are stable in the simplified environment discussed in Section 3.2, their slow dynamics causes high sensitivity with respect to the eccentricity of the binary orbit.

Differently from the previous candidate trajectories, most retrograde interior orbits are extremely robust, as shown in Fig. 13. Failure is almost surely avoided for  $x_0$  ranging from about 0.47 to 0.73 km, i.e.,

$$P_{failure}(\mathbf{r}_0(x_0), \dot{\mathbf{r}}_0(x_0), t_S = 30 \text{ day}) = 0 \quad \forall x_0 \in [0.47, 0.73] \text{ km},$$

which makes this region safe with respect to the uncertainty sources considered, and a very good candidate for the AIDA mission. Although the real trajectory can considerably drift from the design orbit, as shown in Fig. 16, it never enters the circumscribing sphere of the attractors during the entire simulation window and for all possible realizations of the uncertainty sources. This robustness is due to the high velocity of the orbits with respect to the corotating frame, which enables an efficient averaging of the gravitational perturbations due to the non-spherical shape of the primary. Fig. 14 discloses that SRP triggers the failure of the largest members of the retrograde interior family. Once again, the initial longitude of the binary orbit is of primary importance, as all failures occur when it is close to 180 deg.

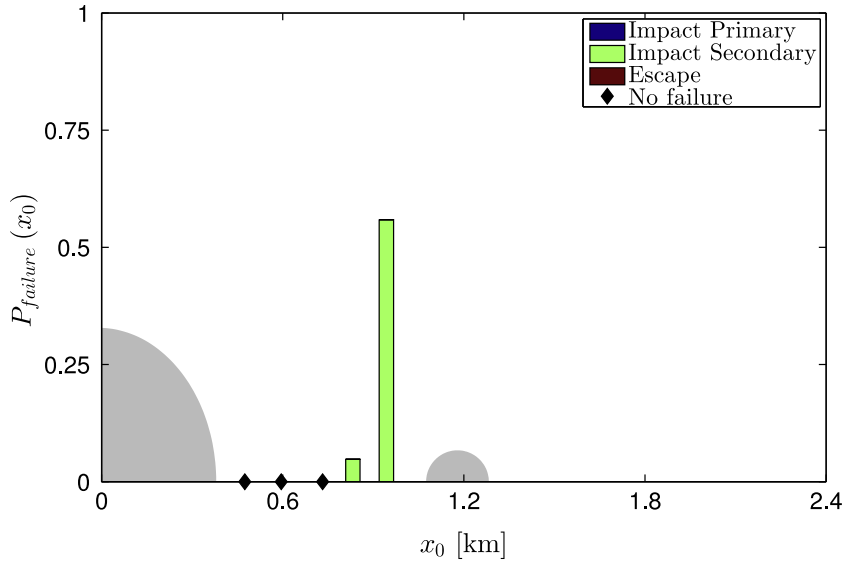


Fig. 13. Probability of failure of retrograde interior orbits.

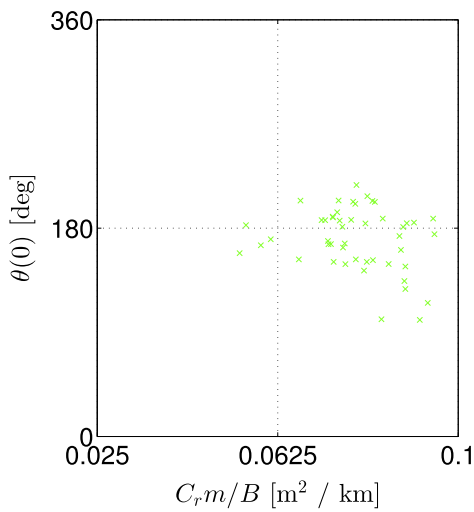


Fig. 14. Failure events of the fourth retrograde interior orbit. The same symbol convention of Fig. 9(b) is used.

Finally, CSO are also seen to fail in most cases, with greater probability of impacting the primary body when the size of the orbit is large (see Fig. 17). In this case, the initial eccentricity of the orbit and the SRP are mainly responsible for the impacts.

In conclusion, only retrograde interior orbits are acceptable for the purposes of the mission.

#### 4.3. Terminator orbits

Various terminator orbits with nominal dimensionless semi-major axis ranging from 1.25 to 7.5 are considered for the MC analysis. During the 400 days propagation window, the heliocentric orbit transits the perihelion, where perturbations due to the Sun reach their maximum.

Fig. 18 shows the probability of failure after 400 days as a function of the semi-major axis. The closest orbit exhibits a very large probability of failure, which is mostly due to

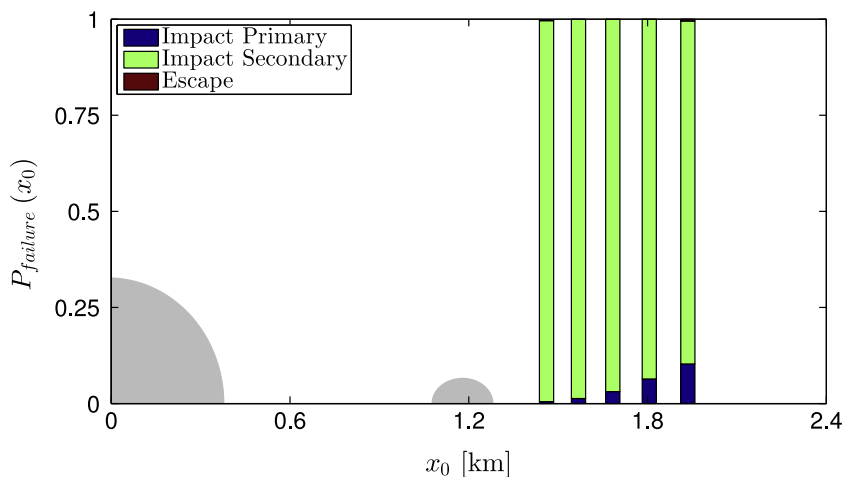


Fig. 15. Probability of failure of retrograde exterior orbits.

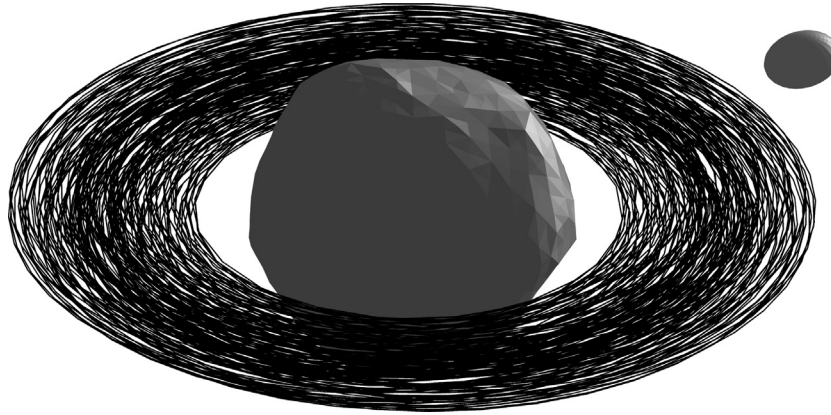


Fig. 16. Sample trajectory of the retrograde interior family. Here,  $e(0) = 0.03$ ,  $\theta(0) = 180$  deg,  $\phi(0) = 10$  deg, and  $B = 20 \text{ kg m}^{-2}$ .

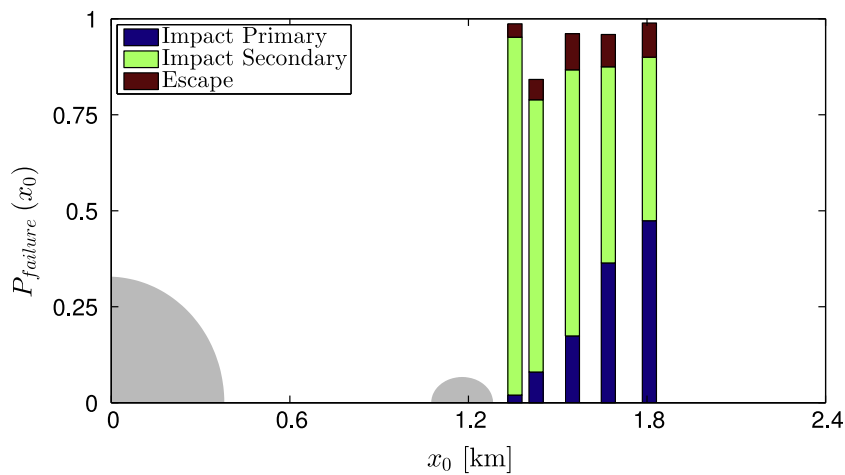


Fig. 17. Probability of failure of CSO.

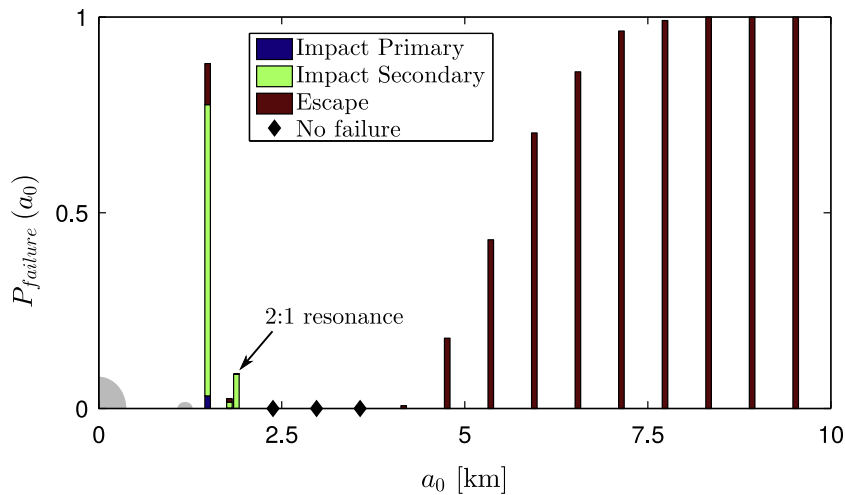


Fig. 18. Probability of failure of terminator orbits.

impacts with the secondary body. Further analysis shows that uncertainty in the magnitude of the SRP, i.e.,  $\frac{c_r}{B}$ , exhibits the largest correlation with the impacting time. Yet, a sharp decrease of  $P_{failure}$  is observed for the second orbit

with  $a \simeq 1.8$  km. Here, the failure happens only in 2.4% of the simulations, with 1.5% due to an impact with the secondary and 0.9% due to an escape. The failure of this orbit is mostly due to insufficient authority of the SRP and, in

lesser extent, to the initial longitude of the binary orbit, as shown on Fig. 19(a).

We also note that the third orbit has much larger failure probability than the second one, i.e., about 9%, although the two orbits have very similar semi-major axis values. This peak is due to a 2 : 1 resonance between the orbital period and the binary's period that causes a growing 'sling' effect that destabilizes the orbit fairly quickly (Fig. 20(a)). As such, resonant orbits should be avoided in the mission design phase.

Orbits with semi-major axis ranging from 2.4 to 3.5 km do not fail almost surely and, as such, they could be considered as safe for the purposes of the AIDA mission. For instance, consider the plots of Figs. 20(b) and 21 illustrating a sample terminator orbit with initial semi-major axis equal to 3.5 km. As it can be seen, frozen orbit conditions are met with satisfactory accuracy. Specifically, the trend of the RAAN accurately follows the heliocentric true anomaly of Didymos (Fig. 21(a)), and the eccentricity is confined between 0.06 and 0.11 (Fig. 21(b)). Also notice that oscillations of the RAAN are slightly amplified in the proximity of the perihelion, i.e., when SRP is maximized. Yet, solar perturbations do not lead to escape from the system as long as the nominal semi-major axis of the spacecraft is less than 4 km.

For larger semi-major axes, SRP effects are strong enough to tear off the satellite from the system, as depicted in Fig. 19(b). In this example, all failures of orbits with semi-major axis equal to 4.7 km occur in correspondence of the crossing of the Didymos perihelion, i.e., after about 200 days.

### 5. Additional results on robust orbits

In Section 4 we identified two robust solutions, namely the planar interior retrograde and the terminator orbits.

Some additional results are now presented for these candidate trajectories of potential interest for the AIDA mission.

#### 5.1. Errors in injection velocity

The safe regions identified in Section 4 are intimately related to the natural dynamics of the Didymos system. Nonetheless, the real-life exploitation of any orbit has to account for uncertainty in the initial states. Quantifying the amount of tolerable uncertainty in the injection velocity would be valuable information for system design purposes. However, this goes beyond the scope of the paper, which is why we limit the present analysis to assessing how much the robustness of the safe solutions deteriorates for a prescribed uncertainty in the injection velocity. Hence, we included in the MC analysis a uniform uncertainty of  $\pm 2$  cm/s in the norm of the initial velocity.

Fig. 22(a) depicts the probability of failure for retrograde interior orbits initialized with this additional source of uncertainty. Differently from the previous results, the probability of impacting with either of the two primaries is now significantly increased. Yet, an optimum value is still attained for  $x$ -crossings close to 0.6 km. Here, the probability of failure is as low as 1.5%.

The same analysis is also repeated for terminator orbits (Fig. 22(b)). Here, the lowest probability of failure is approximately 6% and it is attained for semi-major axis close to 3 km. Nevertheless, 2 cm/s uncertainty is an extremely pessimistic bound for terminator orbits as it represents 17% of the initial orbital velocity. In addition, we note that the minimum failure time occurs after about 50, 150, and 85 days for the terminator orbits with semi-major axes 2.4, 3.0, and 3.5 km, respectively (Fig. 23). This amount of time enables the possibility to formulate and apply orbital corrections in a real-life scenario. Also notice that most of the trajectories at 3.0 km and 3.5 km fail when Didymos is approaching the perihelion and for large injec-

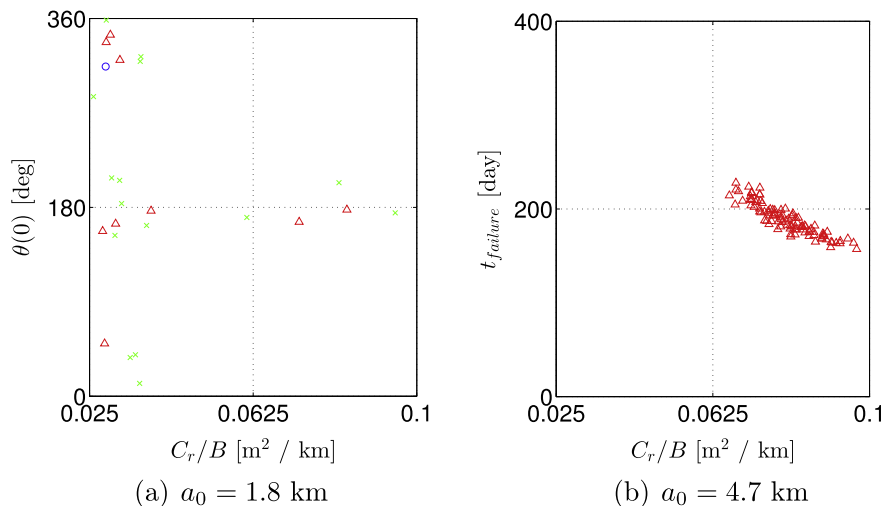


Fig. 19. Failure events of the seventh terminator orbit. The same symbol convention of Fig. 9(b) is used.

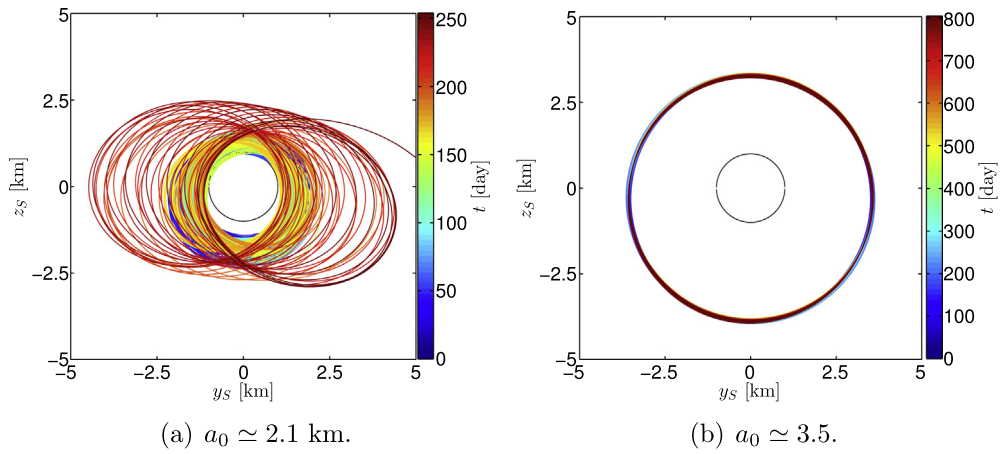
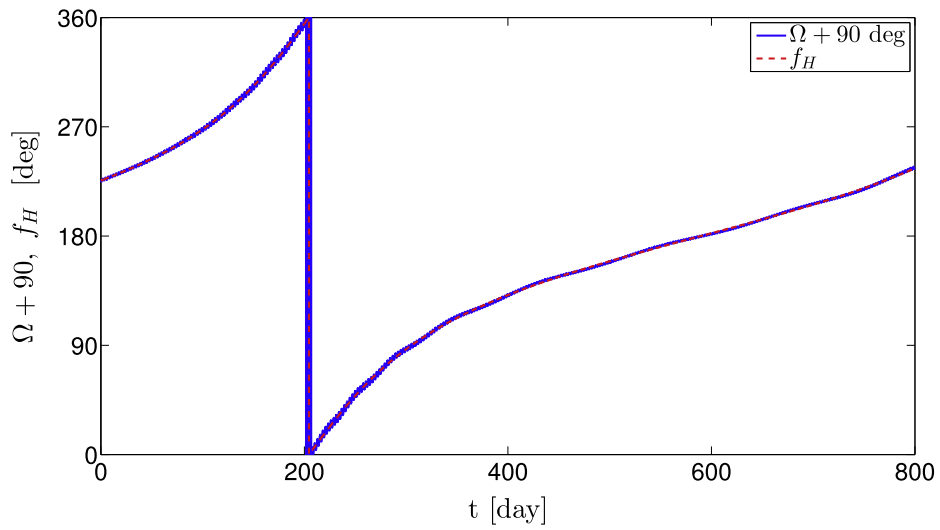
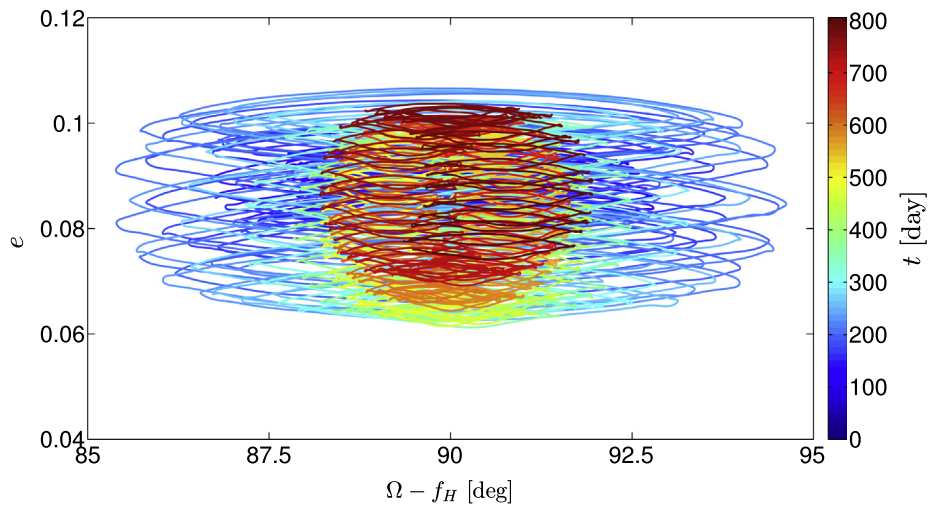


Fig. 20. Sample trajectories of the terminator orbits as seen from the Sun direction. The dotted line denotes the sphere with radius equal to the Didymos semi-major axis.

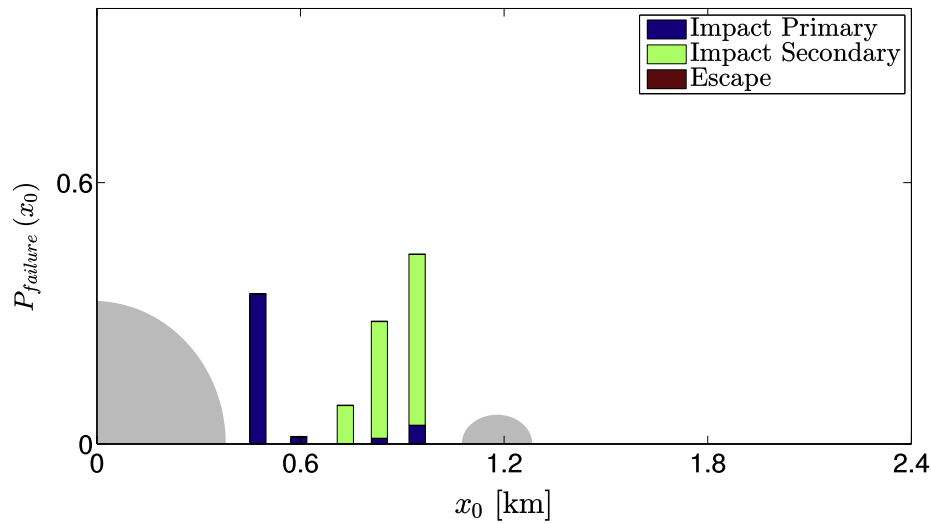


(a) Terminator orbit's RAAN and heliocentric true anomaly.

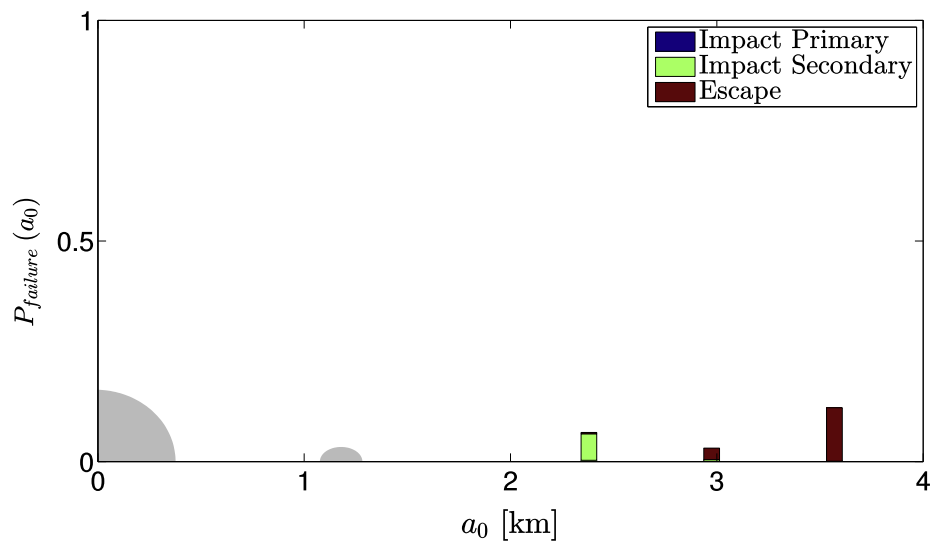


(b) Terminator orbit's RAAN and eccentricity.

Fig. 21. Perturbed frozen terminator orbit. The initial semi-major axis is equal to 3.5 km.



(a) Interior retrograde orbits.



(b) Terminator

Fig. 22. Failure probability by adding  $\pm 2$  cm/s uniform uncertainty to the norm of the injection velocity.

tion errors that increase the relative velocity of the spacecraft with respect to the binary asteroid.

### 5.2. Inclined interior retrograde orbits

Although very close to the primary body, planar interior orbits are not the best candidates for gravity measurements as they lack information on the non-equatorial field. Hence, this paragraph is aimed at investigating the effects of orbital inclination on this orbital family.

To fulfill this task, we model the inclination and initial RAAN of the spacecraft as uniformly distributed random variables in the range  $[90, 180]$  deg and  $[0, 360]$  deg, respectively, and repeat our Monte Carlo analysis. The results of our investigation are shown in Fig. 24 and illustrate that the probability of failure for inclinations larger than

163 deg is still below 1%. As such, inclined interior retrograde orbits should be considered as safe and of scientific interest for the purposes of the AIDA mission due to their capability of sensing most of the primary’s gravitational field.

## 6. Conclusions

This paper offered a numerical investigation of the Didymos dynamical environment. After computing and assessing the robustness of various families of periodic orbits, two safe solutions were identified, which may be of use for the forthcoming AIDA mission. The first are frozen terminator orbits, which ensure global coverage of the binary system and are suitable for communication purposes. The second is the family of planar inner retrograde

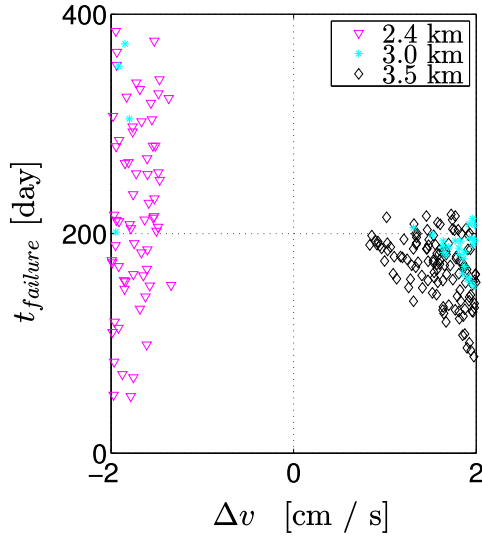


Fig. 23. Time of failure of the safe terminator orbits as a function of the initial injection velocity error. Triangles, stars, and diamonds refer to the cases  $a = 2.4$  km,  $a = 3.0$  km, and  $a = 3.5$  km, respectively.

orbits, which allows for thorough inspections of the main body. A moderate inclination can be safely added to the latter orbits to enhance the sensing of the primary's gravitational field.

### Acknowledgements

This work was partially supported by the Belgian National Fund for Scientific Research (FNRS) and by the John Hopkins University Applied Physics Laboratory.

### Appendix A. Reference frames

The following is a list of reference frames used by the propagator.

Inertial frame,  $I$ , is centered at the Sun and oriented such that the  $\hat{X}_I$  unit vector is pointing towards the ver-

nal equinox,  $\hat{Z}_I$  is perpendicular to the ecliptic plane, and  $\hat{Y}_I = \hat{Z}_I \times \hat{X}_I$  completes the right-handed triad. Heliocentric perifocal frame,  $H$ , is centered at the Sun and oriented such that  $\hat{X}_H$  points towards the perihelion of the binary asteroid eccentric orbit about the Sun,  $\hat{Z}_H$  is perpendicular to the orbital plane of Didymos, and  $\hat{Y}_H = \hat{Z}_H \times \hat{X}_H$  completes the right-handed triad. The transformation from coordinates in  $\mathcal{I}$  to coordinates in  $\mathcal{H}$  is

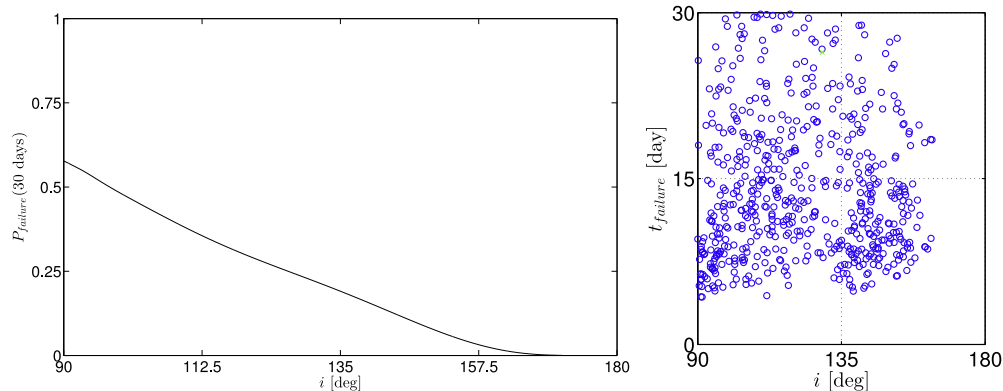
$$\begin{aligned}\hat{X}_H &= (\cos \omega_H \cos \Omega_H - \sin \omega_H \sin \Omega_H \cos i_H) \hat{X}_I \\ &\quad + (\cos \omega_H \sin \Omega_H + \sin \omega_H \cos \Omega_H \cos i_H) \hat{Y}_I \\ &\quad + \sin \omega_H \sin i_H \hat{Z}_I, \\ \hat{Y}_H &= -(\sin \omega_H \cos \Omega_H + \cos \omega_H \sin \Omega_H \cos i_H) \hat{X}_I \\ &\quad + (-\sin \omega_H \sin \Omega_H + \cos \omega_H \cos \Omega_H \cos i_H) \hat{Y}_I \\ &\quad + \cos \omega_H \sin i_H \hat{Z}_I, \\ \hat{Z}_H &= \sin \Omega_H \sin i_H \hat{X}_I - \cos \Omega_H \sin i_H \hat{Y}_I + \cos i_H \hat{Z}_I,\end{aligned}$$

where  $i_H$ ,  $\Omega_H$ , and  $\omega_H$  are the heliocentric inclination, longitude of ascending node, and argument of perihelion of Didymos, respectively.

Pseudo-inertial frame,  $P$ , is centered at the barycenter of the binary system and oriented such that  $\hat{X}_P$  points towards the ascending node of the secondary body at epoch,  $\hat{Z}_P$  is parallel to the pole of the system, and  $\hat{Y}_P = \hat{Z}_P \times \hat{X}_P$  completes the right-handed triad. The transformation from coordinates in  $\mathcal{I}$  to coordinates in  $\mathcal{P}$  is

$$\begin{aligned}\hat{X}_P &= -\sin \lambda \hat{X}_I + \cos \lambda \hat{Y}_I \\ \hat{Y}_P &= -\cos \lambda \sin \beta \hat{X}_I - \sin \lambda \sin \beta \hat{Y}_I + \cos \beta \hat{Z}_I, \\ \hat{Z}_P &= \cos \lambda \cos \beta \hat{X}_I + \sin \lambda \cos \beta \hat{Y}_I + \sin \beta \hat{Z}_I,\end{aligned}$$

where  $\lambda$  and  $\beta$  are the ecliptic longitude and latitude of the pole, respectively. Furthermore, observed that both the orbital momentum of the secondary body and the rota-



(a) Probability of failure after 30 days as a function of the orbital inclination.

(b) Failure events.

Figure 24. Failure of the inclined interior retrograde orbits with  $x$ -crossing equal to 0.5.

tional axes of the primaries are assumed to be parallel to  $\hat{\mathbf{Z}}_P$  as discussed in Section 2.

Co-rotating frame,  $\mathcal{C}$ , is centered at the barycenter of the binary system and oriented such that  $\hat{\mathbf{Z}}_C$  is parallel to  $\hat{\mathbf{Z}}_P$ ,  $\hat{\mathbf{X}}_C$  is toward the line joining the barycenter of the attractors, and  $\hat{\mathbf{Y}}_P = \hat{\mathbf{Z}}_P \times \hat{\mathbf{X}}_P$  completes the right-handed triad. The transformation from coordinates in  $\mathcal{P}$  to coordinates in  $\mathcal{C}$  is

$$\begin{aligned}\hat{\mathbf{X}}_C &= \cos \theta \hat{\mathbf{X}}_P + \sin \theta \hat{\mathbf{Y}}_P, \\ \hat{\mathbf{Y}}_C &= -\sin \theta \hat{\mathbf{X}}_P + \cos \theta \hat{\mathbf{Y}}_P, \\ \hat{\mathbf{Z}}_C &= \hat{\mathbf{Z}}_P,\end{aligned}$$

where  $\theta$  denotes the true longitude of the secondary body.

Body-fixed frame of the primary,  $\mathcal{B}_1$ , is centered at the barycenter of the primary body and oriented such that  $\hat{\mathbf{Z}}_1$  is parallel to the pole of the system, and

$$\begin{aligned}\hat{\mathbf{X}}_1 &= \cos \vartheta \hat{\mathbf{X}}_P + \sin \vartheta \hat{\mathbf{Y}}_P, \\ \hat{\mathbf{Y}}_1 &= -\sin \vartheta \hat{\mathbf{X}}_P + \cos \vartheta \hat{\mathbf{Y}}_P,\end{aligned}$$

where  $\vartheta = \omega_1(t - t_0) + \vartheta_0$ . Here,  $\omega_1$  and  $\vartheta_0$  denote the spin rate of the primary body and the phase of the  $\mathcal{B}_1$  frame at epoch, respectively.

Body-fixed frame of the secondary,  $\mathcal{B}_2$ , is centered at the barycenter of the secondary body and oriented such that  $\hat{\mathbf{X}}_2$ ,  $\hat{\mathbf{Y}}_2$ , and  $\hat{\mathbf{Z}}_2$  are toward the minimum, medium, and maximum axes of inertia of the tri-axial ellipsoid, respectively. The transformation from coordinates in  $\mathcal{B}_2$  to coordinates in  $\mathcal{C}$  is

$$\begin{aligned}\hat{\mathbf{X}}_2 &= \cos \phi \hat{\mathbf{X}}_C + \sin \phi \hat{\mathbf{Y}}_C, \\ \hat{\mathbf{Y}}_2 &= -\sin \phi \hat{\mathbf{X}}_C + \cos \phi \hat{\mathbf{Y}}_C, \\ \hat{\mathbf{Z}}_2 &= \hat{\mathbf{Z}}_C,\end{aligned}$$

where  $\phi$  is the libration angle shown in Fig. 2.

## References

- Arnold, V.I., Kozlov, V.V., Neishtadt, A.I., 1993. *Mathematical Aspects of Classical and Celestial Mechanics*. Springer Nature. <http://dx.doi.org/10.1007/978-3-642-61237-4>.
- Baresi, N., Scheeres, D.J., Schaub, H., 2016. Bounded relative orbits about asteroids for formation flying and applications. *Acta Astronaut.* 123, 364–375. <http://dx.doi.org/10.1016/j.actaastro.2015.12.033>.
- Bellerose, J., Scheeres, D.J., 2005. Periodic orbits in the vicinity of the equilateral points of the restricted full three-body problem. In: *AAS/AIAA Astrodynamics Specialist Conference*, Lake Tahoe, CA.
- Bellerose, J., Yano, H., Scheeres, D.J., 2009. Solar radiation pressure perturbations at binary asteroid systems. *Adv. Astronaut. Sci.* 135, 747–764.
- Benner, L.A.M., Margot, J., Nolan, M.C., et al., 2010. Radar imaging and a physical model of binary asteroid 65803 Didymos. In: *Bulletin of the American Astronomical Society*, p. 1056.
- Brozović, M., Benner, L.A., Taylor, P.A., et al., 2011. Radar and optical observations and physical modeling of triple near-earth asteroid (136617) 1994 CC. *Icarus* 216 (1), 241–256. <http://dx.doi.org/10.1016/j.icarus.2011.09.002>.
- Cheng, A.F., Atchison, J., Kantsiper, B., et al., 2015. Asteroid impact and deflection assessment mission. *Acta Astronaut.* 115, 262–269. <http://dx.doi.org/10.1016/j.actaastro.2015.05.021>.
- ESA, 2015. *Asteroid Impact Mission: Didymos Reference Model AD3. Technical Report*. European Space Agency.
- Gabern, F., Koon, W.S., Marsden, J.E., 2006. Parking a spacecraft near an asteroid pair. *J. Guid., Control, Dyn.* 29 (3), 544–553. <http://dx.doi.org/10.2514/1.15138>.
- Howell, K.C., 1984. Three-dimensional, periodic, ‘halo’ orbits. *Celest. Mech.* 32 (1), 53–71. <http://dx.doi.org/10.1007/bf01358403>.
- Margot, J.L., Nolan, M.C., Benner, L.A.M., et al., 2002. Binary asteroids in the near-earth object population. *Science* 296, 1445–1448. <http://dx.doi.org/10.1126/science.1072094>.
- McMahon, J.W., Scheeres, D.J., 2013. Dynamic limits on planar libration-orbit coupling around an oblate primary. *Celest. Mech. Dyn. Astron.* 115 (4), 365–396. <http://dx.doi.org/10.1007/s10569-012-9469-0>.
- Naidu, S.P., Benner, L.A.M., Brozovic, M., et al., 2016. Shape and spin state of Didymos. In: *The 4th Workshop on Binaries in the Solar System*.
- Naidu, S.P., Margot, J.L., Taylor, P.A., et al., 2015. Radar imaging and characterization of the binary near-earth asteroid (185851) 2000 DP107. *Astron. J.* 150 (2), 54. <http://dx.doi.org/10.1088/0004-6256/150/2/54>.
- Ostro, S.J., Margot, J.L., Benner, L.A.M., et al., 2006. Radar imaging of binary near-earth asteroid (66391) 1999 KW4. *Science* 314 (5803), 1276–1280. <http://dx.doi.org/10.1126/science.1133622>.
- Pravec, P., Scheirich, P., Kušnirák, P., et al., 2016. Binary asteroid population. 3. Secondary rotations and elongations. *Icarus* 267, 267–295. <http://dx.doi.org/10.1016/j.icarus.2015.12.019>.
- Pravec, P., Scheirich, P., Kušnirák, P., et al., 2006. Photometric survey of binary near-earth asteroids. *Icarus* 181, 63–93. <http://dx.doi.org/10.1016/j.icarus.2005.10.014>.
- Scheeres, D.J., 1994. Dynamics about uniformly rotating triaxial ellipsoids: applications to asteroids. *Icarus* 110 (2), 225–238. <http://dx.doi.org/10.1006/icar.1994.1118>.
- Scheeres, D.J., 1999. Satellite dynamics about small bodies: averaged solar radiation pressure effects. *Adv. Astronaut. Sci.* 47, 25–46.
- Scheeres, D.J., 2012. *Orbital Motion in Strongly Perturbed Environments*. Springer-Verlag, Berlin. <http://dx.doi.org/10.1007/978-3-642-03256-1>.
- Scheeres, D.J., Bellerose, J., 2005. The restricted hill full 4-body problem: application to spacecraft motion about binary asteroids. *Dyn. Syst.* 20 (1), 23–44. <http://dx.doi.org/10.1080/1468936042000281321>.
- Shampine, L.F., Reichelt, M.W., 1997. The MATLAB ODE suite. *SIAM J. Sci. Comput.* 18 (1), 1–22. <http://dx.doi.org/10.1137/s1064827594276424>.
- Shannon, C.E., 1948. A mathematical theory of communication. *Bell Syst. Tech. J.* 27 (4). <http://dx.doi.org/10.4135/9781412959384.n229>.
- Szebehely, V., 1967. *Theory of Orbits*. Elsevier. <http://dx.doi.org/10.1016/b978-0-12-395732-0.x5001-6>.
- Werner, R.A., Scheeres, D.J., 1996. Exterior gravitation of a polyhedron derived and compared with harmonic and mascon gravitation representations of asteroid 4769 Castalia. *Celest. Mech. Dyn. Astron.* 65 (3), 313–344. <http://dx.doi.org/10.1007/bf00053511>.